Chemical Engineering Journal 150 (2009) 344–351

Contents lists available at ScienceDirect

Chemical Engineering Journal

journal homepage: www.elsevier.com/locate/cej

Numerical simulation of mixing process of gas–liquid impinging jet in ballast water discharge pipe

Gu Jianlong[a,*], Zhang Zhitao[a], Song Chunlian[a,b], Yang Xianli[a]

[a] Environmental Engineering Institute, Dalian Maritime University, Dalian 116026, China
[b] Heilongjiang Jixi University, Security and Environmental Department, Jixi 158100, China

ARTICLE INFO

Article history:
Received 11 July 2008
Received in revised form 24 December 2008
Accepted 8 January 2009

Keywords:
Gas–liquid impinging jet
Confined crossflow
Eulerian–Eulerian two-equation model
Gas volume fraction
Weighted coefficient of variation
Ballast water treatment

ABSTRACT

When a gas–liquid turbulent jet with hydroxyl free radicals is jetted into a ballast water discharge pipe to kill the invasive microbes, there is a challenge for hydroxyl free radicals to contact a large number of microbes in ballast water. In this paper, the Eulerian–Eulerian two-equation model is employed to simulate the mixing process of gas–liquid being jetted into the ballast water crossflow. The results show that the upstream wall-surface vortices lead to counter-rotating scarf vortex pairs (CVSPs) at downstream in confined crossflow, which enhance the mixing process. However, it is hard for the gas in the downstream wall-surface jet to diffuse due to the fact that the CVSPs have no influence on the downstream wall-surface jet. Therefore, the higher the momentum ratio is, the lower the value of weighted coefficient of variation of gas volume fraction at outlet is, however, when the momentum ratio is constant, the weighted coefficient of variation first drops and then goes up with increasing diameter ratio.

1. Introduction

The introduction of invasive marine species into new environments via ships' ballast water and other carriers has been identified by Global Environment Facility (GEF) as one of the four greatest threats to the world's oceans. This problem has become the focus of Marine Environment Protection Committee (MEPC) of International Maritime Organization (IMO). At present, the advanced oxidation technology based on hydroxyl free radicals is a promising technology for ballast water treatment [1–3]. Since hydroxyl free radicals are of high oxidation efficiency [4], the transport pipelines of ballast water can be used as a "pipeline reactor", namely, the harmful microbes can be killed in ballast water discharge process.

The process of online ballast water treatment must take account of the characteristics of ballast water and hydroxyl free radicals. First of all, a vast volume of ballast water is discharged in a short time. For example, 75,000 tons of ballast water carried by a 175,000-ton bulk are emptied with two 2500-ton ballast pump in 15 h, and the velocity is 2.5 m/s in pipe with the diameter of 600 mm; secondly, low dosage of hydroxyl free radicals is adequate for killing a large number of harmful invasive marine microbes because of its strong oxidization; thirdly, since the life span of hydroxyl free radicals is short, the uniform mixing period must be short enough to ensure plenty of time for killing invasive organisms. Thus, the uniform degree of mixing determines the effect of removing the organisms by hydroxyl free radicals in a limited length of ballast water discharge pipe. An online treatment equipment must be designed under the condition of having no influence on the ballast water discharge; hence, the effective channel mixing method and proper pipe length must be figured out to optimize the performance of the online treatment equipment.

In recent decades, studies on the single-, multi-nozzle or narrow-gap free jet vertically jetting into crossflow found that the most significant characteristic is the forming of counter-rotating vortex pairs (CVPs) like kidneys [5–7], leading to uniform mixing and good mass transfer [8]. The CVPs aforementioned are induced from a flow pattern of turn jet [9], which does not penetrate the ambient crossflow or impinge pipe wall. Although existing in a long distance, the CVPs are not easy to swell in radial direction because of the limitation of pipe wall and the weak momentum ratio (jet-to-crossflow). The shear stress between CVPs and crossflow is not strong so that a "mixed death zone" exists between CVPs and pipe wall, where the jet hardly mixes with crossflow. While the jet penetrates the ambient crossflow and impinges pipe wall, upstream wall-surface vortices are formed at upstream. When bypassing the jet body, upstream wall-surface vortices lead to counter-rotating scarf vortex pairs abbreviated as CVSPs, which can suck crossflow with more force and result in better radial mixing [5,10]. Therefore, the strong entrainment characteristics of CVSPs can be used to strengthen the uniform degree of mixing between impinging jet and crossflow. The flow of ship's ballast water treatment is shown in Fig. 1.

* Corresponding author. Tel.: +86 411 81743628; fax: +86 411 84727681.
E-mail address: jianlong.gu@gmail.com (Gu Jianlong).

1385-8947/$ – see front matter.
doi:10.1016/j.cej.2009.01.020

Nomenclature

$C_{1\epsilon}$, C_2	constants in Realizable $k-\epsilon$model
C_1, C_μ	parameters in Realizable $k-\epsilon$ model
$C_v(C_{v,w})$	the (weighted) nonuniform degree coefficient
d, D	diameters of jet and main pipe, respectively
$\vec{g}$	acceleration of gravity (m/s^2)
G_k	the generation of turbulent kinetic energy (J/m^3 s)
$\vec{F}_q$	an external body force (N)
$\vec{F}_{lift,q}$	a lift force (N)
$\vec{F}_{Vm,q}$	a virtual mass force (N)
I	turbulent intensity
$\bar{\bar{I}}$	the unit tensor
k_q	turbulent kinetic energy (m^2/s^2)
P	the pressure shared by all phase (Pa)
R_d	jet-to-pipe diameter ratio $R_d = d/D$
R_m	jet-to-pipe momentum ratio $R_m = (\rho_j d^2 v_j^2/\rho_c D^2 v_c^2)$
R_e	Reynolds number
$\vec{R}_{pq}$	an interaction force between phase (N)
S	a ratio of standard deviation
$\vec{v}_q$	velocity vector (m/s)
x_i	a mean value of each small distribution interval
$\bar{x}_i$	a mean value of whole distribution interval
y_i	a percentage of distribution of gas volume fraction

Greek symbols

α_q	volume fraction
ϵ_q	dissipation energy (m^2/s^3)
λ_q	bulk viscosity (kg/m s)
μ_q	shear viscosity (kg/m s)
$\mu_{t,q}$	eddy viscosity (kg/m s)
$\sigma_{k,q}$, $\sigma_{\epsilon,q}$	constants in Realizable $k-\epsilon$ model
ν_q	kinematic viscosity (m^2/s)
ρ_q	density (kg/m^3)
$\bar{\bar{\tau}}_q$	stress–strain tensor
$\bar{\bar{\tau}}_q'$	Reynolds stress tensor

Subscripts

c, j	crossflow, jet
g, L	gas, liquid
p, q	phase p th, q th

When ballast water pumped by pump 1 flows through the discharge pipe, part of the water is sucked by booster pump 2 as motive fluid. At throat of mixer 3, the water is accelerated to suck the specific gas. The specific gas is produced from device 4 , a dielectric barrier discharge reactor, where oxygen and water vapour can be ionized to produce large number of hydroxyl free radicals. Furthermore, the specific gas is broken into small bubbles at throat of mixer and then disperses into the motive fluid. At last, the gas–liquid with hydroxyl free radicals vertically jets back into ballast water. In the process of gas–liquid jet mixing with crossflow, the harmful invasive microorganisms are killed by hydroxyl free radicals.

Although single-, multi-nozzle or narrow-gap jet vertically jetting into crossflow [5–7] and the flow in T-type[11,12], have been studied, little literature on multiphase impinging jet was reported because the properties of impinging jet in crossflow and multiphase flow are too complicated. In this paper, the Eulerian–Eulerian two-equation model is employed to simulate the mixing process of gas–liquid impinging into the ballast water crossflow. The results show that the wall-surface vortices come into being at upstream and will lead to counter-rotating scarf vortex pairs (CVSPs) at downstream. The formation and development of CVSPs enhance the process of jet mixing with crossflow, but, it is hard for the gas in the downstream wall-surface jet to diffuse. Therefore, increasing momentum ratio and pipe diameter ratio results in different changing trends of weighted coefficient of variation at outlet.

2. Mathematical formulations

For phase q th of a multiphase turbulent flow, the governing equations of mass, momentum and Realizable $k-\epsilon$ turbulence model are

Continuity equation:

$$\nabla \cdot (\alpha_q \rho_q \vec{v}_q) = 0 \tag{1}$$

Momentum equations:

$$\nabla \cdot (\alpha_q \rho_q \vec{v}_q \vec{v}_q) = -\alpha_q \nabla P + \nabla \cdot \bar{\bar{\tau}}_q + \alpha_q \rho_q \vec{g} + (\vec{F}_q + \vec{F}_{life,q} + \vec{F}_{Vm,q}) + \sum_{p=1}^{n} R_{pq} \tag{2}$$

Phase stress–strain tensor:

$$\bar{\bar{\tau}}_q = \alpha_q \mu_q (\nabla \vec{v}_q + \nabla \vec{v}_q^T) + \alpha_q \left(\lambda_q - \frac{2}{3}\mu_q\right) \nabla \cdot \vec{v}_q \bar{\bar{I}} \tag{3}$$

Reynolds stress tensor:

$$\bar{\bar{\tau}}_q' = -\frac{2}{3}(\rho_q k_q + \rho_q \mu_{t,q} \nabla \cdot \vec{v}_q)\bar{\bar{I}} + \rho_q \mu_{t,q} (\nabla \vec{v}_q + \nabla \vec{v}_q^T) \tag{4}$$

Turbulent viscosity:

$$\mu_{t,q} = \rho_q C_\mu \frac{k_q^2}{\epsilon_q} \tag{5}$$

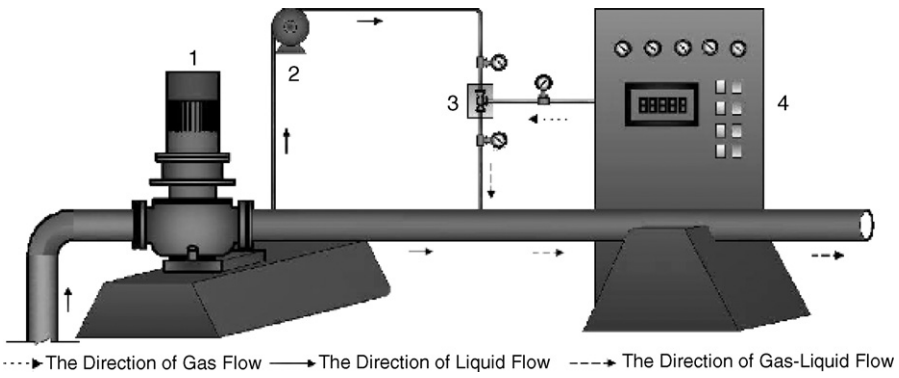

Fig. 1. Flow chart of ballast water treatment: 1, ballast water pump; 2, booster pump; 3, jet mixer; 4, free radicals-generated apparatus.

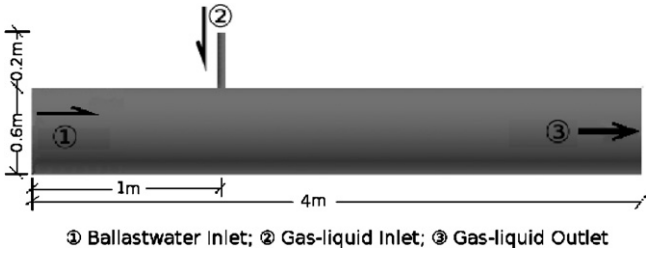

Fig. 2. Schematic diagram of tee pipe.

Turbulent kinetic energy k_q:

$$\nabla \cdot (\alpha_q \rho_q k_q \vec{v}_q) = \nabla \left[\left(\mu_q + \frac{\mu_{t,q}}{\sigma_{k,q}} \right) \right] + G_{k,q} - \rho_q \epsilon_q \tag{6}$$

The rate of dissipation of turbulent kinetic energy ϵ_q:

$$\nabla \cdot (\alpha_q \rho_q \varepsilon_q \vec{v}_q) = \nabla \left[\left(\mu_q + \frac{\mu_{t,q}}{\sigma_{\epsilon,q}} \right) \right] + \rho_q C_1 S_q \epsilon_q - \rho_q C_2 \frac{\epsilon^2}{k_q + \sqrt{\nu_q \epsilon_q}} \tag{7}$$

where, α_q, ρ_q, $\vec{v}_q$ are volume fraction, density and velocity of phase q th, respectively; λ_q and μ_q are bulk viscosity and shear one; $\vec{g}$ is acceleration due to gravity; K_{pq} is coefficient of the momentum exchange term for turbulent flows; $\vec{F}_q$, $\vec{F}_{lift,q}$ and $\vec{F}_{Vm,q}$ are the external body force, lift force and virtual mass force, respectively. Eqs. (1)–(7) constitute the closure formulations for the current simulation. The model constant $C_{1\epsilon,q}$, C_2, $\sigma_{k,q}$ and $\sigma_{\epsilon,q}$ have been established to ensure that the model performs well for certain canonical flows. The model constants are:

$$C_{1\epsilon,q} = 1.44, \qquad C_2 = 1.9, \qquad \sigma_{k,q} = 1.0, \qquad \sigma_{\epsilon,q} = 1.2$$

And the others in these equations can be referred to FLUENT 6.3 User's Guide.

At the same time, the volume fractions of all phases sum to unity:

$$\sum_{q=1}^{n} \alpha_q = 1 \tag{8}$$

Namely, fractions of all phases must sum to unity in every control volume. Therefore, if the control volume is full of liquid, then $\alpha_L = 1$. Similarly, if it is full of gas, then $\alpha_g = 1$. In all cases, the gas is assumed to be inert and behave as a homogeneous phase.

3. Computation domain/grid and boundary conditions

The impinging jet will bring out many various vortices including shear vortex, scarf vortex, wake vortex and so on, which affect markedly the flow characteristics in the vicinity of impinging point. And the impinging jet flow shows strong three-dimensional properties, so a 3D computation domain is taken into consideration. Parameters of the 3D computation domain are: the main pipe with the length of 4 m, the diameter of 0.6 m, the lateral pipe with a length of 0.2 m crosses vertically the main pipe at 1 m from left inlet. A schematic diagram of tee-pipe is shown in Fig. 2.

Fig. 3 shows the structure grids of computation zone.

The velocity of water flow is 2.5 m/s for the left velocity-inlet of main pipe, and the velocity of gas–liquid flow is a series of values for the velocity-inlet of lateral pipe. The pressure is 3.5 atm for the outlet of main pipe. Assumed to be fully developed pipe flow, the turbulent intensity at inlet and outlet can be estimated with Eq. (9)[13].

$$I_{g(L)} = 0.16(Re)^{-1/8} \tag{9}$$

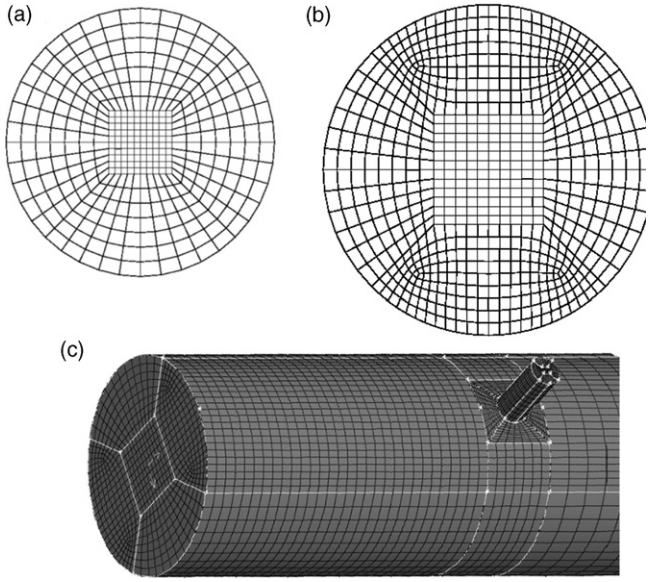

Fig. 3. Grids distribution of inlet and wall. (a) Grids of branch inlet; (b) grids of main pipe; (c) wall-grids of junction.

The wall boundary conditions are of no-slip boundary conditions. For the evaluation of wall effect on turbulence, the near-wall treatment employs STANDARD WALL FUNCTIONS [14]. There is no heat transfer between liquid and wall, so the ENERGY EQUATION is not worked out.

4. Simulation cases

The major parameters used in the process of the numerical simulations are given in Table 1.

All numerical simulations are carried out at ambient temperature. The simulations are realized by Fluent code, which is a commercial software including the broad physical model and has been applied to industrial applications ranging from air flow over an aircraft wing to combustion in a furnace, from bubble columns to glass production, from blood flow to semiconductor manufacturing, from clean room design to wastewater treatment plants, and which is a leader in multiphase modeling technology. The second-order scheme is employed except for volume fraction equation using quick scheme.

5. Results and discussion

5.1. Analysis of the pathlines of different momentum ratios

Fig. 4 shows the development of pathlines of gas–liquid confined impinging jet with different momentum ratios. The legend represents the flow time of pathlines, the time unit is second (s). Developing from inlet to outlet, the pathlines in blue indicate short time while the red indicate long time. The pathline profiles, with a little difference of maximum of flow time from inlet to outlet, are put together to share the same legend, such as $R_m = 1.60$ and $R_m = 6.40$, $R_m = 2.30$ and $R_m = 3.14$, $R_m = 4.09$ and $R_m = 5.18$.

Due to the limitation of wall and crossflow, the development of pathlines is different in the vicinity of impinging point. When R_m

Table 1
Summary of simulation conditions.

Momentum ratio	1.60	2.30	3.14	4.09	5.18	6.40
Pipe radius ratio	0.09	0.14	0.19	0.24	0.28	–

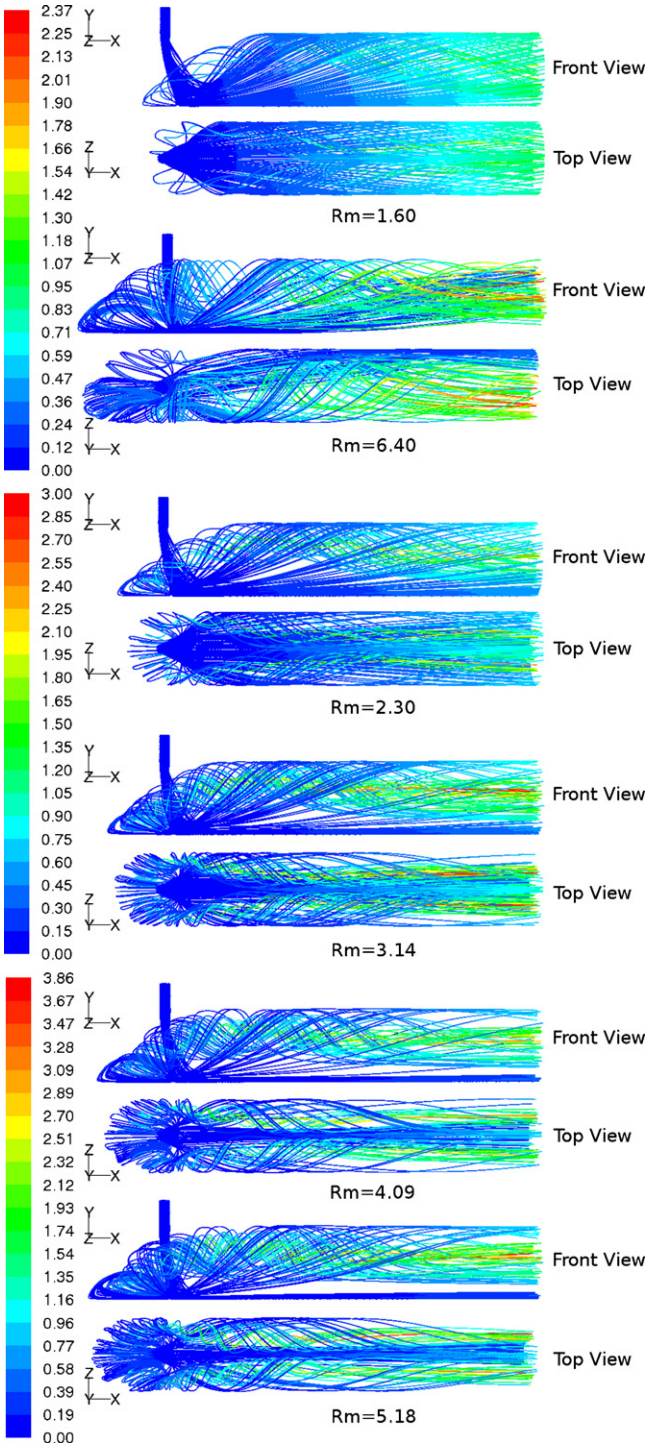

Fig. 4. Distribution of pathlines with different momentum ratios at $R_d = 0.14$.

ranges from 1.60 to 5.18 at $R_d = 0.14$, the pathlines appear symmetry distribution from top view. However, when $R_m = 6.40$, the pathlines are no longer symmetrical as mentioned in the reference [10], and shown in Fig. 4.

First of all, the wall-surface jet around impact point comes into being on account of wall interruption, but its development is different because of the limitation of wall and the crossflow. At windward side of jet, wall-surface jet plugs in the space between wall and crossflow. The jet's energy of flowing upstream decays due to the drag of crossflow. When the jet's energy disappears somewhere, the wall-surface jet turns back with crossflow. However, a little part of this jet returns to the upstream wall-surface jet, so a type of vortices called upstream wall-surface vortices are induced at last. We could clearly note that, when momentum ratio increases from 1.60 to 3.14, namely, the higher the momentum ratio is, the more upward the vortex centre is and the greater the vortex height is, but the increscent trend is not obvious as momentum ratio changes from 3.14 to 5.18. After bypassing the jet body, the upstream wall-surface vortices develop into scarf vortices . At downstream cross-section, the scarf vortices are in the form of a pair of counter-rotating scarf vortices (CVSPs).

At the same time, the ambilateral pathlines of jet body developing downstream in a confined pipe is different from pathlines in a unconfined space [10]. In a confined pipe, the ambilaterial pathlines climb along the wall when pathlines extend downstream. With momentum ratio changing from 1.60 to 5.18, the height of climbing pathlines grows greater, and so is the bending strength. When the clambing pathlines reach the top and collide into each other, they convene towards the bottom again and form the secondary jet flow. The secondary jet can enhance the vortex intensity of CVSPs.

Additionally, with R_m increasing from 1.60 to 5.18, the maximum of the residence time grows greater and is proportional to the vortex intensity. Namely, the existence of CVSPs can enhance the residence time of jet flow. Nevertheless, the non-blue pathlines mainly exist at the center of CVSPs and the curvature of pathlines is greater than that of the blue. The above-mentioned changing characteristics are displayed in Fig. 4.

In Fig. 4 for $R_m = 6.40$, the pathlines appear asymmetrical distribution, that is to say, the upstream wall-surface vortices and scarf vortices move one side, whose ability of sucking crossflow is greatly enhanced. While a small part of pathlines of jet and pathlines of downstream wall-surface jet distribute on the other side, whose curvature is flat and the ability of sucking crossflow is weakened. Since the process of sucking crossflow is asymmetric, the location of pathline distribution generates deflexion in confined pipe, which is different from the distribution in unconfined space [10]. Comparing with $R_m = 5.18$, the residence time of pathlines is greatly shortened. For example, the maximum of residence time is 3.86 s at $R_m = 5.18$ but only 2.37 s at $R_m = 6.40$.

5.2. Analysis of the pathlines of different diameter ratios

The higher the momentum ratio is, the stronger the interaction and mixing between jet and crossflow are, thus the development of pathlines of different diameter ratios is analyzed at constant momentum ratio. In order to discuss in depth the interaction of pathlines between main pipe and lateral pipe, the birth sites of pathlines are put on a few straight lines at two inlets. For example, the y-coordinate of straight lines at main pipe inlet lies in $0, \pm 0.25$m, respectively, and the center lines along x- and z-coordinates at lateral inlet are selected. Interaction pathlines are shown in Fig. 5.

The stagnation spot of impinging jet varies with R_d ranging from 0.09 to 0.28. For example, the pathlines of jet hardly skew downstream at $R_d = 0.09$ but skew downstream evidently at $R_d = 0.28$. The foregoing results could be explained in this way that the larger the contacting area between jet and crossflow is, the greater the acting force on jet imposed by crossflow is, and simultaneously the smaller the flow rate of the upstream wall-surface vortices is.

The pathlines start from $y = 0.25$ m of main pipe inlet and maintain horizontal development without being affected by upstream wall-surface vortices. When pathlines are close to jet, the partial pathlines confronting jet body get sharply curve downward owing to the interruption and drag force by jet, and then is involved in upstream wall-surface vortices. The part close to the pathlines confronting jet body also bends down and forms boundary layer of downstream wall-surface jet, but this part does not mix well with

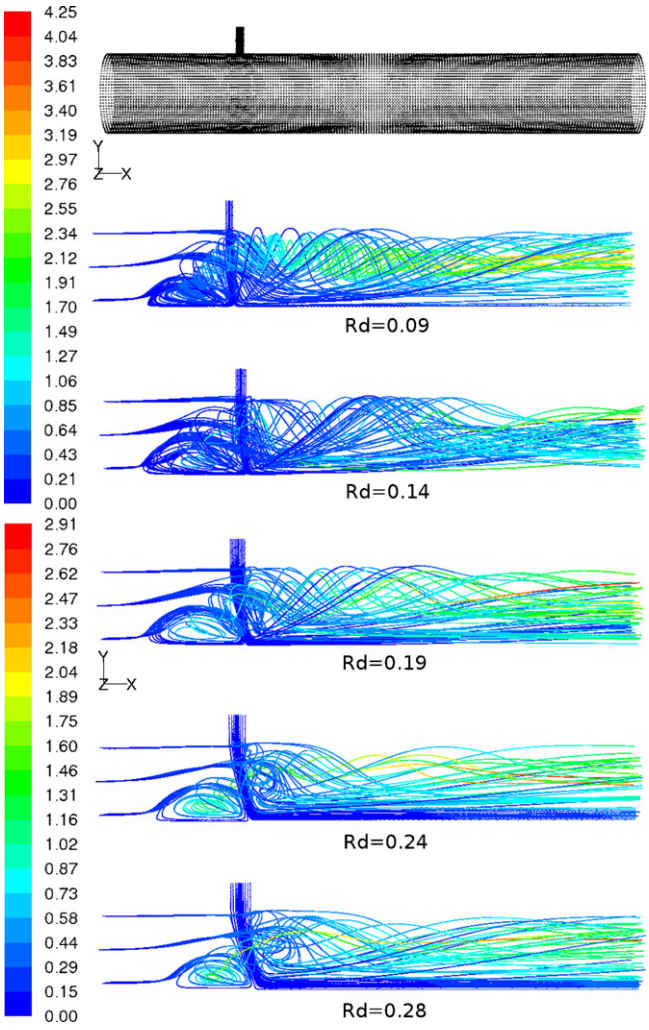

Fig. 5. Distribution of pathlines with different diameter ratios at $R_m = 6.40$.

jet, that is, the gas volume fraction is the smallest in this zone. The segment far away from the pathlines confronting jet body bends upward due to the low pressure behind nozzle, and then in a distance goes downward, the pathlines also go sharply down and form the boundary layer of downstream wall-surface jet. The color of pathlines transfer from blue at upstream to blue-green at downstream. Comparing with the legend, it is known the residence time of those pathlines is short because they depend only on the initial velocity of the inlet.

As for pathlines starting from $y = 0$, the horizontal part of which is shorter than that of those starting from $y = 0.25$ m. The pathlines hump upward after meeting the upstream wall-surface vortices, and then bend down because of the drag force of jet. However, the pathlines bypassing the jet body mainly adhere to outer sphere of CVSPs rather than form boundary layer of downstream wall-surface jet. Additionally, the color of pathlines changes from blue to green. It is shown that the residence time is longer than the former's on account of the influence of CVSPs.

For pathlines starting from $y = -0.25$ m, the interaction with upstream wall-surface vortices is evident. The pathlines cohere and interwine with upstream wall-surface vortices, and then develop into CVSPs after bypassing the jet. Moreover, these pathlines are not affected by downstream wall-surface jet. The pathlines in the center of CVSPs is non-blue, whose flowing time is much greater than others. For example, when $R_d = 0.09$, the flowing time actually reaches 4.25 s.

All in all, as for the crossflow, pathlines below $y = 0$ are mainly sucked by upstream wall-surface vortices at upstream, and sucked by CVSPs at downstream. The lower the y value of pathline location is, the stronger the influence of upstream wall-surface vortices is, hence the crossflow falling in this zone easily mix with jet flow. Contrary to that, pathlines beyond $y = 0$ are hardly affected by upstream wall-surface vortices and CVSPs, so the greater the value of y is, the less the influence is. Those pathlines form boundary layer of downstream wall-surface jet, where the gas volume fraction of this zone is the smallest. Additionally, when mometum ratio is constant, the velocity increases with decreasing jet diamter, the stronger the upstream wall-surface vortices are, the longer the residence time of pathlines in center of vortices is.

Therefore, the intensity of upstream wall-surface vortices and CVSPs is a key factor for the mixing degree. For example, increasing intensity of vortices leads to greater mixing degree because the residence time of jet in the vortices is longer and the ability of sucking the crossflow is greater, that is, the prolonged residence time ensures the sufficient contact betwen jet and crossflow, which results in better gas dispersion at last.

5.3. Uniform degree of mixing at outlet

The contour map and weighted variation coefficient of gas volume fraction are analyzed to decide the optimal momentum and diameter ratio, which can realize high degree of mixing between jet and crossflow in a limited pipe.

Fig. 6 shows the contour map of gas volume fraction under different momentum ratios at $R_d = 0.14$ and the legend shows the gas volume fraction without dimension. The contour map is symmetrical when $R_m \leq 4.09$, but is partial asymmetrical at $R_m = 5.18$ and is obvious asymmetrical at $R_m = 6.40$. Although the contour map grows asymmetrical when $R_m \geq 5.18$, the mixing process still comply with certain laws, in other words, the greater the momentum ratio is, the stronger the influence of CVSPs on gas distribution gets, at the same time, and leading to greater gas volume in the downstream wall-surface jet. The part of jet flow clambering along wall encounters and compresses at upper, and then converges towards bottom again, which results in secondary jet flow and increasing the vortex intensity of CVSPs. It is also noted that gas–liquid fluid will cover the pipe wall to the outlet. When the momentum ratio increases, the secondary jet flow is closer to bottom, but its head bifurcates again like an "anchor" or an inversing "mushroom" together with CVSPs. Since the vortex intensity of CVSPs gets stronger when R_m increases from 1.60 to 5.18, the vortex center of CVSPs grows more evident in contour map. In addition, as the momentum ratio increases, the gas volume in the downstream wall-surface jet increases, but the zone between CVSPs and downstream wall-surface jet reduces.

Fig. 7 shows that the contour map of gas volume fraction under different diameter ratios at $R_m = 6.40$. The distribution of contour map is symmetrical except for $R_d = 0.14$ and $R_d = 0.19$. With R_d increasing, the thickness of downstream wall-surface jet grows thicker than the former. The thickness can be seen through the longitudinal and cross-sectional contour map at $R_d = 0.09$, $R_d = 0.24$ and $R_d = 0.28$, but merely through the cross-sectional contour map for $R_d = 0.14$ and $R_d = 0.19$. The degree of skewness of jet body can also be embodied by contour map at the longitudinal profile, of which its change tendency and cause have been mentioned in pathlines and will not be repeated here. Comparing Fig. 6 with Fig. 7, it is noted that the upstream wall-surface vortices change a little with increasing diameter ratio as shown in Fig. 7, but the vortex height is greater and the vortex center is farther away from the impinging point with growing momentum ratio as shown in Fig. 6. In addition, when $R_d = 0.24$ and $R_d = 0.28$, there is a new phenomena that the CVSPs isolates from secondary jet flow.

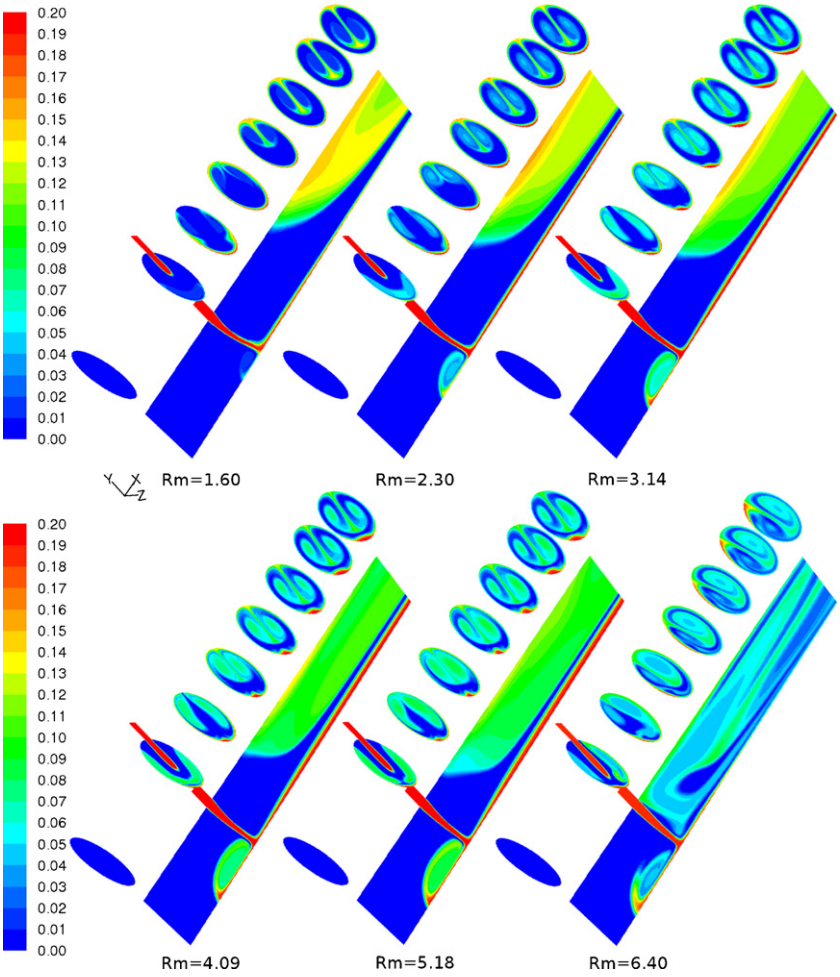

Fig. 6. Longitudinal and cross-sectional contour map of gas volume fraction at $R_d = 0.14$.

All in all, in the momentum-dominated near field, namely, before the jet impinges on the wall, the jet-induced velocity is significantly greater than the ambient current, and the jet is only slightly affected by the crossflow. Thus the mixing is similar to that of a momentum jet in still fluid. However, after the jet impinges on the wall, the upstream wall-surface vortices form and enhance the mixing degree between jet and crossflow. At downstream side of the jet, the upstream wall-surface vortices become the CVSPs which can remain in long distance downstream. As expected, the mixing is greatly enhances by the CVSPs in the far-field.

The degree of mixing could be demonstrated by the histogram of gas volume fraction at outlet, but it is not easy to distinguish among different cases in the condition of changing momentum ratio and diameter ratio. Currently, for statistical analysis of the histogram of gas volume fraction at outlet, the standard tecnnique is the coefficient of variation ($C_v = (S/\bar{x}) \times 100\%$). The coefficient of variation is the ratio of standard deviation of component concentration ($S = \sqrt{(1/(n-1))\sum_{i=1}^{n}(x_i - \bar{x})^2}$) to its mean concentration ($\bar{x} = (1/n)\sum_{i=1}^{n} x_i$). However, the percentage of each small interval is not considered. So the percentage had better be taken as a weighted factor. Therefore, the weighted coefficient of variation is calculated by the formula as follows:

$$C_{v,w} = \frac{\sqrt{(\sum_{i=1}^{n}(x_i - \bar{x})^2 \times y_i)/(n-1)}}{\bar{x}} \times 100\% \quad (10)$$

where, $C_{v,w}$ is the weighted coefficient of variation; x_i and $\bar{x}$ are the mean value of each small distribution interval and the whole distribution interval of gas volume fraction, respectively. y_i is the percentage of each small distribution interval of gas volume fraction.

Fig. 8 shows the variation trend of weighted coefficient of variation with different momentum ratios. The declining trend of weighted coefficient of variation is critical from 1.60 to 2.30 but slows down from 2.30 to 6.40, the reason of which is that more jet flow are turned into the downstream wall-surface jet with increasing momentum ratio, and this part is of no effect by CVSPs so that less gas is diffused in time. Therefore, when the momentum ratio equals 6.40, the value of weighted coefficient of variation is 12.8%, which could result in the rapid and short-distance mixing between jet and crossflow.

Fig. 9 shows the changing trend of weighted coefficient of variation with different diameter ratios. Comparing with the former's, the trend is greatly different from Fig. 8. For example, when the momentum ratio is constant, as the diameter ratio gets larger, the weighted coefficient of variation first drops down, and then goes up again. The valley value of coefficient 12.8% is reached when diameter ratio equals 0.14. Before the valley value, the coefficient drops off sharply; and after the valley value, the coefficient climbs sharply from 0.14 to 0.28. The weighted coefficient of variation rises due to the force on the jet by crossflow gets stronger with increasing diameter ratio, and more jet flow forms the downstream wall-surface jet just like the case of increasing momentum ratio at a constant diameter ratio.

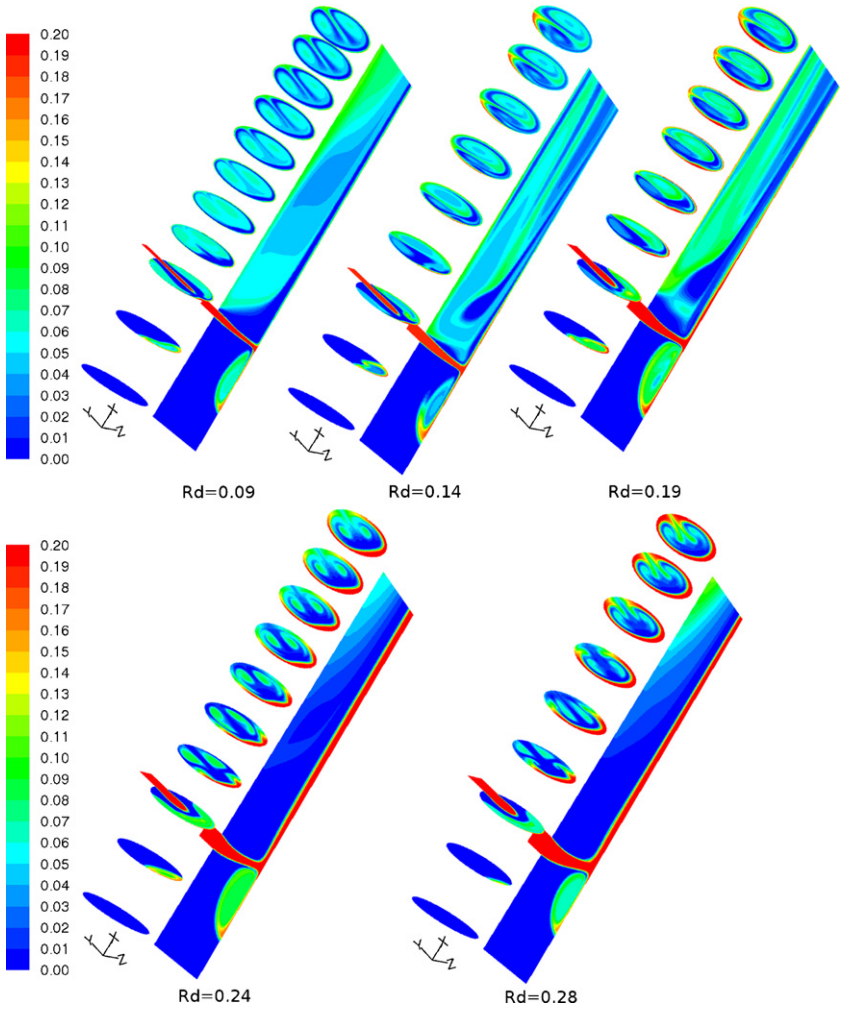

Fig. 7. Longitudinal and cross-sectional contour map of gas volume fraction at $R_m = 6.40$.

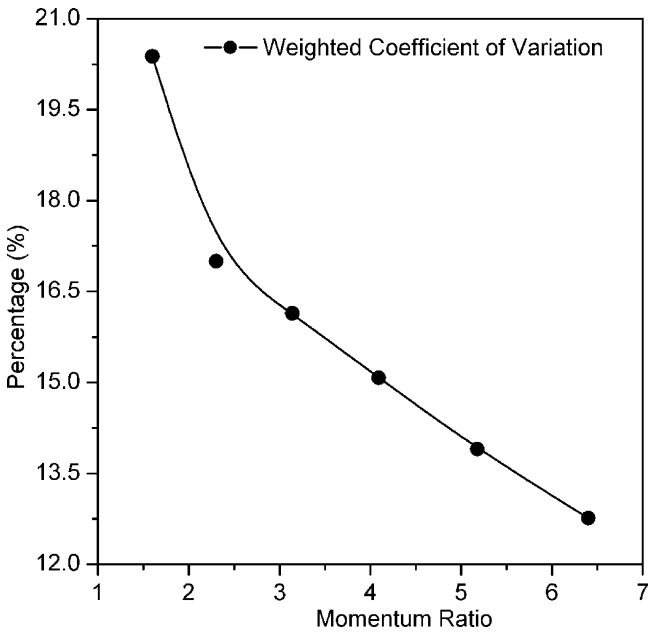

Fig. 8. Weighted coefficient of variation of gas volume fraction at $R_d = 0.14$.

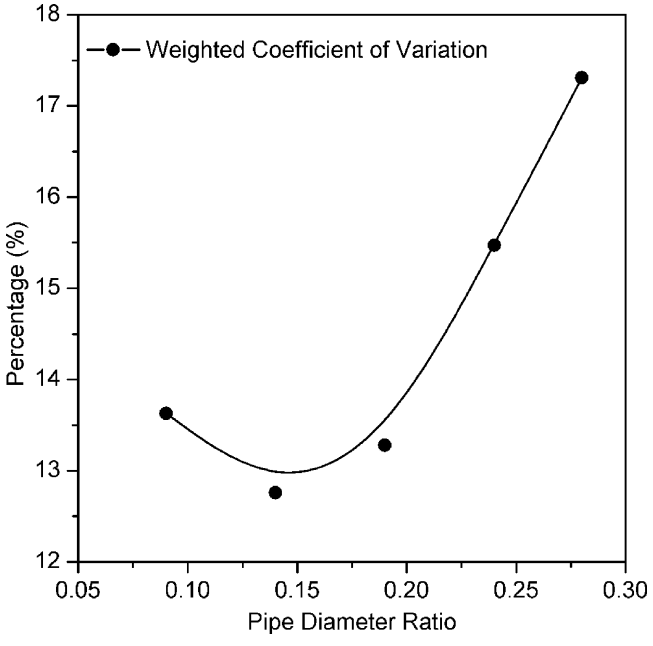

Fig. 9. Weighted coefficient of variation of gas volume fraction at $R_m = 6.40$.

6. Conclusion

The Eulerian–Eulerian two-equation model is employed to simulate the mixing process of gas–liquid being jetted into the ballast water crossflow. Some specific conclusion are summerized as follows:

(1) Analyzing the profiles of mixture pathlines shows that upstream wall-surface vortices are the major cause for counter-rotating scarf vortex pairs (CVSPs) at downstream in confined crossflow, and the secondary jet increases the vortex intensity of CVSPs. The vortices enhance the mixing process, in other words, the complete and uniform mixing mainly depends on the CVSPs at downstream.
(2) It is difficult for the gas to diffuse in the downstream wall-surface jet flow without influence of CVSPs.
(3) Analysis of contour map and weighted variation coefficient of gas volume fraction at outlet shows that the higher the momentum ratio is, the lower the weight coefficient of variation is. Especially, when the pathlines or contour maps are asymmetric, though the residence time in pipe grows shorter, the degree of mixing is much greater.
(4) Therefore, within reasonable span of energy dissipation, the optimal momentum ratio is greater than or equal to 6.40 when the diameter ratio is 0.14. When the momentum ratio equals 6.40, the optimal value of R_d is 0.14.

Experiments shall be performed to further clarify the effect of impinging jet on the degree of mixing, particularly to collect more data on the influence of increasing momentum ratio and diameter ratio. At the same time, experiments results shall be consistent with numerical simulations, and prove the transition boundary condition from symmetric to asymmetric distribution of gas volume fraction.

Acknowledgments

This work was supported by Key Projects in the National Science & Technology Pillar Program in the Eleventh Five-year Plan Period (grant no. 2006BAC11B06) and by the Program for New Century Excellent Talents in University (grant no. NCET-05-0296).

References

[1] M.D. Bai, Z.T. Zhang, M.D. Bai, Effects of hydroxyl radicals on introduced organisms of ship's ballast water based micro-gap discharge, Plasma Sci. Technol. 9 (2007) 206–210.
[2] X.Y. Bai, Z.T. Zhang, M.D. Bai, Killing of invasive species of ship's ballast water in 20t/h system using hydroxyl radicals, Plasma Chem. Plasma Proc. 25 (2005) 41–54.
[3] Z.T. Zhang, M.D. Bai, Y. Xiao, Treating ballast water with hydroxyl radical on introduced organisms, Chinese J. Ocean. Limnol. 24 (2006) 161–167.
[4] X.M. Ma, Q. Song, C. Hu, Y.Z. Wang, J.H. Qu, Disinfection and degradation of 2,4-DCP with UV-radiation and on-line ozone in drinking water treatmeat, Chinese J. Environ. Sci. 23 (2002) 57–61.
[5] H. Joseph, W. Lee, C.P. Kuang, G.Q. Chen, Structure of a turbulent jet in a crossflow—effect of jet-crossflow velocity, China Ocean Eng. 16 (2002) 1–20.
[6] D.A. Compton, J. Johnston, Streamwise vortex production by pitched and skewed jets in a turbulent boundary layer, AIAA J. 30 (1992) 640–651.
[7] J.M. Hu, H.L. Han, Numerical study on behavior of finite length inclined positived buoyant jets in crossflow, J. Hydrodyn. 19 (2004) 275–280.
[8] I.A. Waitz, D.S. Underwood, Effect of heat release on streamwise vorticity enhanced mixing, AIAA J. (1995) 2471.
[9] M.H. Seyed, Y.K. Kazuhisa, H. Hashizume, Classification of turbulent jets in a T-junction area with a 90-deg bend upstream, Int. J. Heat Mass Transfer (2008) 2444–2454.
[10] Y. Zhang, Experimental and numerical investigations on the vortical structures of an impinging jet in crossflow, Shanghai University, Shanghai, 2005, p. 51.
[11] I. Turunen, A. Soleymani, E. Kolehmainen, Numerical and experimental investigations of liquid mixing in T-type micromixers, Chem. Eng. J. 135 (2008) S219–S228.
[12] G. Baker, W.W. Clark, B.J. Azzopardi, J.A. Wilson, Transient effects in gas–liquid phase separation at a pair of T-junctions, Chem. Eng. Sci. 63 (2008) 968–976.
[13] Fluent Inc., FLUENT User's Guide. Fluent Inc., 2006.
[14] B.E. Launder, D.B. Spalding, The numerical computation of turbulent flows, Comput. Methods Appl. M. 3 (1974) 269–289.